



ARTICLE

DOI: [10.1038/s42005-018-0069-5](https://doi.org/10.1038/s42005-018-0069-5)

OPEN

Competition between green self-trapped-exciton and red non-bridging-oxygen emissions in SiO₂ under interband excitation

Alberto Paleari ¹, Francesco Meinardi¹, Sergio Brovelli ¹ & Roberto Lorenzi¹

The knowledge advancement in the physics of silicon dioxide has promoted ground-breaking progress, from microelectronics to fibre optics. However, the SiO₂ exciton decay mechanism is still mostly unrevealed. Here, we analyse the temperature dependence of interband-excited luminescence and the reflectivity by means of synchrotron radiation on a wide selection of SiO₂ materials. This enables us to decouple the band-to-band recombination steps from non-radiative decay pathways that typically mask the relaxation mechanisms. We show that band-to-band excitations decay into two competitive correlated channels leading to green and red luminescence so far ascribed to independent transitions. Here we discuss the assignment to a dual relaxation route involving either 'free' or 'interacting' non-bridging-oxygen sites. Such an interpretation suggests an explanation for the elusive non-bridging-oxygen centres in quartz. The reflectivity spectra finally demonstrates a general relationship between exciton spectral position and bandwidth in SiO₂ and clarifies the role of disorder in exciton localization.

¹ Department of Materials Science, University of Milano - Bicocca, via Cozzi 55, Milan 20125, Italy. Correspondence and requests for materials should be addressed to A.P. (email: alberto.paleari@unimib.it)

In any material system, the answer to what is the exciton configuration and whether exciton self-trapping occurs, deals with the intimate nature of the aggregation state and its coupling with the electronic excitations. This aspect becomes particularly relevant when one faces the task of describing the radiation–matter interactions able to produce functional modifications in materials with wide technological spread, such as silicon dioxide. Despite its consolidated role in contemporary pillar technologies, SiO₂ is continuing to stimulate fundamental^{1–3} and applied studies in microelectronics⁴ and photonics^{5,6} and to generate new cutting-edge scientific fields, such as optical 5D information storage⁷, nanowire sensing⁸ and ultra-strong nanofibres⁹. Fundamentally, many consolidated and emerging applications of SiO₂ involve radiation–matter interactions, either in the material processing or in its operative conditions. For example, above-gap excitation of SiO₂ can lead to structural changes and to modifications of the optical and the dielectric response, which have an impact in fibre optics and photonics¹⁰, microelectronics¹¹ and even in nuclear waste management¹². For this reason, several studies have investigated the mechanisms of radiation-induced defect formation in SiO₂¹³, revealing their relation to exciton decay via bond dissociation or via the formation of vacancy–interstitial sites¹⁴. Nevertheless, the configuration of the SiO₂ exciton is not understood in all its decay steps and current knowledge is still mostly based on paradigmatic pioneering experiments of X-ray-excited optically detected magnetic resonance in quartz¹⁵ and parallel measurements of transient optical absorption, density change and light emission by electron-beam irradiation^{16,17}. Such experiments, supported by coeval calculations and more recent molecular dynamics studies^{18–21}, indicate that the SiO₂ exciton manifests itself in a self-trapped exciton (STE) configuration^{22,23}, whose formation includes two main players: a three-fold coordinated silicon atom, an oxygen atom displaced from the regular coordination site and a neighbouring oxygen centre with which it forms an unspecified chemical bond. More detailed models of the STE configuration invoke the formation of a peroxy linkage^{13,15} or a bond between a non-bridging-oxygen (NBO) and a nearby bridging oxygen, as supported by spectroscopic studies of band-to-band excited luminescence²⁴.

The luminescence spectrum is arguably one of the main sources of experimental information on the exciton decay in SiO₂, together with parallel studies with different spectroscopic techniques²⁵. From these evidences, the blue-green spectral region was recognized as the region of the STE light emission, mainly characterized by long lifetime resulting from the triplet state (few μ s at 300 K and about 1 ms at cryogenic temperatures^{25,26}) and excitation in the intrinsic band-to-band region. In fact, X-ray-, electron-beam-^{17,24,26} and two-photon-excited photoluminescence spectra²⁶, typically show red and green-blue emissions in silica and green-blue luminescence in quartz. The green-blue component at 2.4–2.7 eV is commonly ascribed to STE and shares the spectral region with defect-related contributions of hydrogen- or alkali-decorated NBOs^{26,27} and oxygen-deficient centres²⁸. These defect-related emissions possess quite long lifetimes, similarly to the STE, and in some conditions with very similar values, from 8 to 12 μ s at 300 K and few 10¹ μ s at 90 K for hydrogen-perturbed NBOs²⁶ to about 10 ms, 112 μ s and 10 μ s for oxygen-deficient twofold coordinated Si, Ge and Sn sites in amorphous SiO₂, respectively, at 300 K²⁹. The red photoluminescence at 1.9 eV is, instead, associated with NBOs, which are amongst the most investigated point defects in silica^{30,31}, with main excitation channels at 2.0 eV, 4.8 eV and 6.8 eV and relatively long lifetime of about 10–20 μ s^{32–34}. Variants with slightly different spectral features due to interactions with nearby functional groups^{26,27} or bridging³⁵ and non-bridging oxygens³⁶ are

also commonly observed. Despite the fundamental role of elementary NBO point defects in bond-breaking events in SiO₂, their red photoluminescence has never been observed in quartz, except for locally amorphized crystals by neutron irradiation^{37,38}. Mainly for this reason, early interpretations of the band-to-band excited photoluminescence spectra did not explicitly consider the NBO emission as a possible contribution to the radiative decay of STEs.

Aim of the present work is to obtain a definite spectral insight into the relationship between NBO and STE, so as to face an unresolved critical point. In fact, despite NBOs are expected to be involved in the STE configuration, whose acknowledged spectral fingerprint is in the blue-green region, the light emission of NBO instead lies in the red and is usually ascribed to stable defects only. Here, by using synchrotron light band-to-band excited photoluminescence experiments conducted over a wide range of temperatures on a comprehensive set of silica specimens obtained through different synthetic methods and treatment conditions, as well as on pristine and neutron-irradiated quartz, we reveal that the band-to-band excited green and red luminescence in silica are not independent transitions, but instead arise from the bifurcation of the decay process of intrinsic excitations into a dual relaxation route involving either ‘free’ or ‘interacting’ NBO configurations. By doing so, our data suggest an explanation for the absence of the red luminescence in untreated quartz and a general relationship between exciton trapping and structural disorder in SiO₂.

Results

Rationale of the experiments. We investigated a set of silica and quartz specimens rationally selected so as to represent the largest variety of SiO₂-based materials currently known (see details in Methods). Such comparative approach is strategic for two main reasons: First, it enables us to distinguish the spectral signatures of the STE decay from different sample-dependent photoluminescence contributions. Second, it identifies the silica variant for which the temperature-controlled photoluminescence is free from non-radiative decay processes, and thus directly unveil the configurational relaxation path of band-to-band excitations. The rationale of the study is depicted in Fig. 1, while Table 1 reports the list and description of the main silica variants considered in the investigation (data on optical absorption and Raman spectra of the full set of samples are reported in Supplementary Figure 1 and Supplementary Table 1).

As regards the use of synchrotron light (energy density < 0.1 J cm⁻² and power density < 0.1 W cm⁻²), such an excitation source is particularly suitable for band-to-band spectroscopy. It removes difficulties that affect studies of the SiO₂ exciton using other types of excitation. First, as far as the photon energy does not exceed two times the band gap, it prevents mechanisms of multiplication of electronic excitations³⁹. Second, synchrotron radiation does not introduce structural perturbations that are instead promoted by exposure to high energy ionizing radiation and particle beams or to intense laser light⁴⁰. While the excitation-induced defect generation cannot, however, be excluded completely, at least in an unstable form⁴¹, the data we present in the next sections in fact confirms that the influence of generated defects is negligible in our experiments.

Synchrotron-excited photoluminescence. In Fig. 2a we report the photoluminescence contour plots at 8 K of four silica variants (namely, p-spr, d-spr, p-cvd and s-spr) as a function of the band-to-band excitation energy, compared with the patterns excited in the sub-band-gap vacuum ultraviolet (VUV) range, which exemplify the variety of optical responses encountered in our

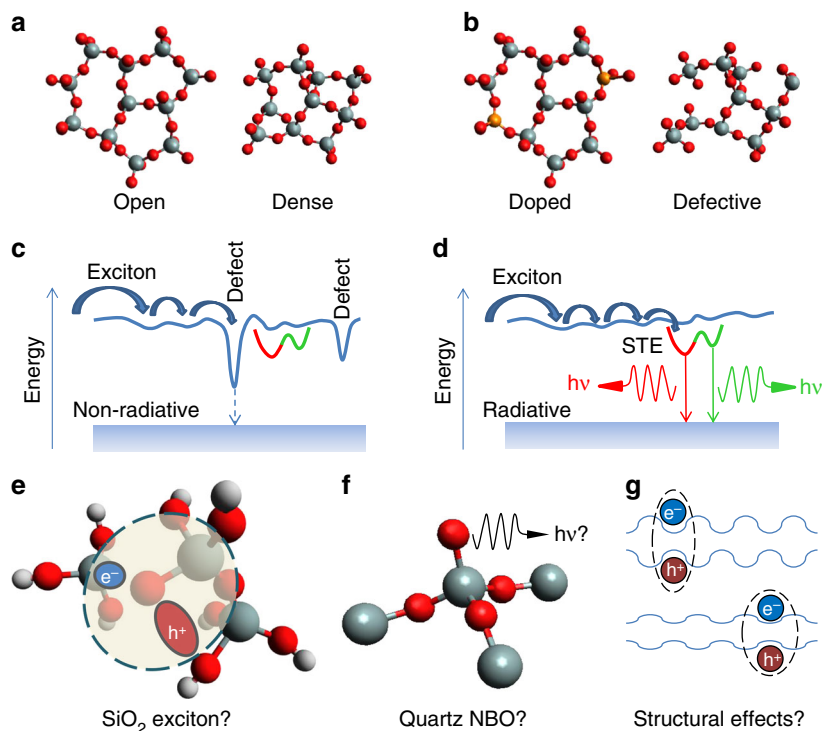


Fig. 1 Rationale of the study. **a** Schematic depiction of the amorphous network of representative silica systems across the continuum of different structural SiO_2 variants, namely the open network by sol-gel synthesis route (open) and the dense packaging of tetrahedral units in fused dry synthetic systems by chemical vapour deposition from SiCl_4 (dense). **b** Schematic depiction of the doped network with heterogeneous dopants substituting for Si (doped), and the defective network resulting from neutron irradiation or incorporation of modifier ions/molecules (defective); silicon atoms are pictured in grey, oxygen atoms in red and heterogeneous dopants in orange). **c** Schematic picture of the decay channels for the band-to-band excited SiO_2 , showing the role of non-radiative decay processes and defects. **d** Radiative decay channels responsible for band-to-band excited photoluminescence when non-radiative decay channels are minimized, highlighting two ubiquitous intrinsic radiative exciton decay channels with emissions in the red and green spectral regions. The study of the radiative decay paths in a SiO_2 system with suppressed non-radiative decay, and the analysis of structure-dependent exciton features in the reflectivity spectra answers longstanding questions on **e**, the structural configuration responsible for the radiative decay of self-trapped-exciton, **f** the elusive nature of NBO in crystalline SiO_2 (quartz), **g** the intimate connection between the material structure and the excitonic spectral features

Table 1 Silica variants. Main categories of investigated silica systems, identified by production method (first column) and perturbation level of the structural network, from nominally pure parent samples (second column) to samples conditioned by doping (third column) or by treatment-induced defects (forth column)

	Undoped	Doped	Defective
Silica by solution-processing route	Pure sol-gel silica (u-spr)	Sn-doped sol-gel silica (s-spr)	Silicon-rich sol-gel silica (d-spr)
Silica by chemical vapour deposition	Pure CVD silica (u-cvd)	Ge-doped CVD silica (g-cvd)	n-irradiated CVD silica (n-cvd)

Sample labels are indicated in brackets

study. Sub-band-gap VUV-excited spectra is dominated by defect-related emissions with excitation bands in the 6.5–8 eV region, ascribable to high excited states of oxygen-deficient centres (ODC) and NBO, with main emissions in the region 2.5–3.2 eV and at 1.9 eV^{13,27–32,34}. This sub-band-gap VUV-excited response is consistent with previous data, mainly showing ODC luminescence excited at about 5 eV, specifically in Sn-doped silica^{29,42}, Ge-doped silica^{29,42,43}, Si-rich silica^{29,44} and silica from chemical vapour deposition (CVD)⁴⁵, either treated and untreated. By contrast, notwithstanding the large structural/compositional differences between the investigated material systems, Fig. 2a reveals a ubiquitous pattern excited above gap, with two spectral contributions always paired to each other and without a reliable relationship with the intensity of sub-band gap excited defect-related emissions: one at ~2.5 eV corresponding to

the STE photoluminescence and one at ~1.9 eV ascribable to NBO-like emission. This fact strongly suggests that these emissions are caused by intrinsic decay paths of interband excitations. We note that similar red and green components are also observed in fractoluminescence spectra of silica⁴⁶, where the double emission is strictly related to intrinsic bond-breaking processes. However, the data in Fig. 2a rule out any strong contribution by defects that in principle could give rise to similar emissions, such as native NBOs and ODCs. In fact, within the investigated materials, the intensity ratio between band-to-band excited and sub-band-gap excited green and red luminescence includes values larger than 1. This outcome is inconsistent with an attribution to defects only, because the excited volume at 10 eV is much smaller (of the order of 10^{-8} cm^3 if the absorption coefficient is 10^5 cm^{-1})^{47,48} than in the spectral region 5–7 eV (of the order of

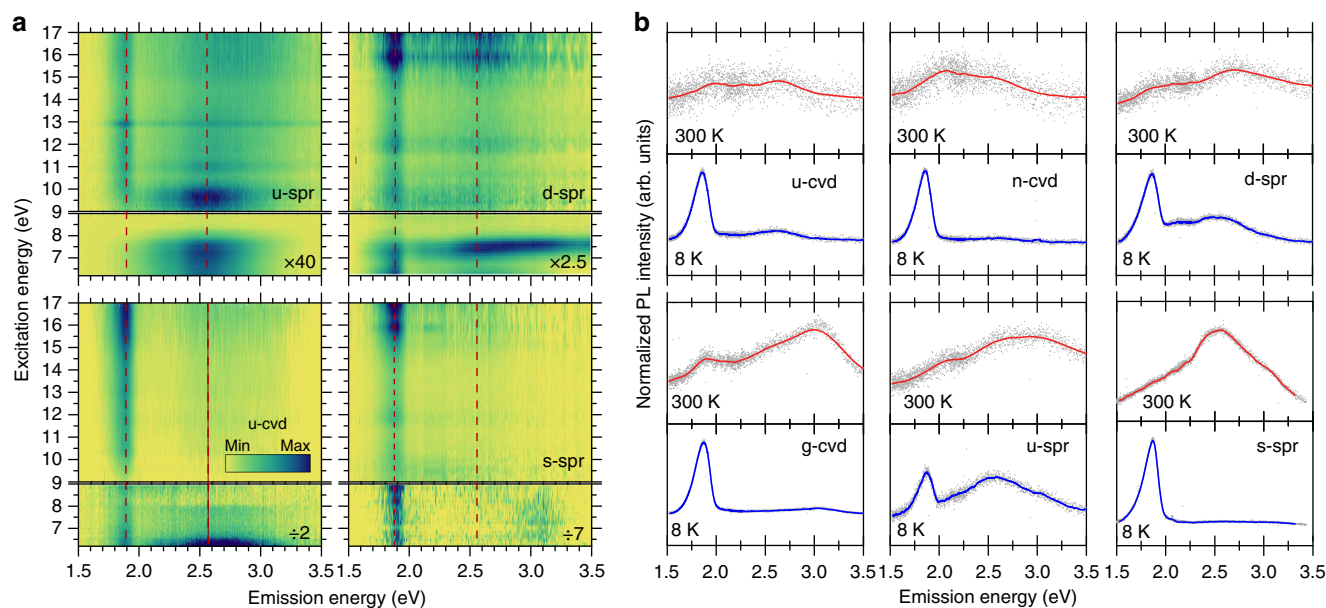


Fig. 2 Band-to-band excitation-emission spectra. **a** Contour plots of light emission spectra at 8 K excited above the band gap energy from 9 to 17 eV and in the sub-band-gap VUV region from 6.3 to 9 eV in fully densified pure sol-gel silica (u-spr), in sol-gel silica synthesized by addition of 1 mol% of $\text{Si}_2(\text{OCH}_3)_6$ as a molecular precursor of Si-Si groups defectiveness (d-spr), in pure synthetic commercial dry silica by chemical vapour deposition (u-cvd), and in fully densified sol-gel silica doped with 0.2 mol% SnO_2 (s-spr); dashed lines are guides for the eye. **b** Comparison between photoluminescence spectra (experimental data in grey, smoothed data in full line) excited at 13.8 eV at 8 K and 300 K in u-cvd, in the same material after neutron irradiation at a fluence of 10^{18} neutrons per cm^2 (n-cvd), in d-spr, in s-spr, in u-spr and in pure synthetic commercial dry silica by chemical vapour deposition with 2 mol% GeO_2 (g-cvd). Additional blue-violet component at 2.7–3.1 eV at 300 K is caused by thermally activated transitions at intrinsic or extrinsic ODCs

10^{-5} cm^3 with an absorption coefficient of few 10^2 cm^{-1})^{49–51}. Therefore, the number of defects that can be directly excited by above-gap one-photon absorption is three orders of magnitude smaller than the number of defects excited below gap. Such a difference cannot be compensated by the different excitation yield in the two spectral regions, since the energy deposited per absorbed photon in our experiments (10^0 – 10^1 eV) and the absorption events per unit time (10^8 – 10^9 photons ms^{-1}) are not expected to provide much more than one secondarily excited defect per absorbed photon. The collected spectra also confirm that above-band-gap excitation does not significantly excite luminescence from surface-related defects such as those observed on porous silica⁵². The excited volume is much thicker than the surface reconstruction layer, and a factor 10^1 – 10^2 greater than the thinner SiO_2 films that were proved to give a bulk response⁴⁸. We indeed estimate (on the basis of VUV absorption and reflectivity data^{49–51}), a radiation attenuation depth in the region 8.5–17 eV ranging from 20 to 200 nm, which correspond to about 10^2 – 10^3 layers of coordination units.

Figure 2b and Supplementary Figure 2 show photoluminescence spectra of all investigated silica variants at 8 K and at room temperature, highlighting the common behaviour across the sample set. Despite the structural/compositional differences, all materials exhibit a similar evolution of their emission spectrum with temperature, showing strong red luminescence at cryogenic temperature that becomes dominated by a green emission at room temperature, disregarding of the absolute thermal quenching of the total intensity.

Deeper details of the temperature effects emerge from Fig. 3. Figure 3a displays the integrated intensity of the red and the green emission bands as a function of temperature, extracted from the respective photoluminescence spectra as shown in Fig. 3b. We notice that, while thermally activated processes cause an essentially monotonic dimming of the red emission in all the

investigated systems (fluctuations are within the experimental uncertainty), the green component in most samples (u-cvd, u-spr, g-cvd and n-cvd in Fig. 3a) shows a markedly non-monotonic behaviour, comprising a gradual decrease with the temperature approaching room conditions. This indicates the occurrence of sample-dependent thermally activated non-radiative mechanisms competing also with the green emission channel. This points to a role of coordination defects, which vary from sample to sample, as non-radiative traps for the silica exciton⁴¹. Accordingly, except for minor fluctuations, the defective d-spr Si-enriched material shows the green emission with a basically monotonic negative trend with increasing temperature. Importantly, parallel to this feature, green emission and red emission too are known to have negligible thermal dependence of the decay kinetics⁵³. Such a feature points to sample-dependent quenching mechanisms that are not caused by competitive decay paths in the emitting system itself, but to factors which influence the number of emitting sites, either before the formation of the excited state or after the radiative transition. Post-transition events were suggested to be the cause of thermal quenching of sub-band-gap excited green emission through the annihilation of transient centres produced by optical excitation⁵³. Band-to-band excitations present a quite different scenario, since the photon energies are not generally resonant with localized defect transitions, but generate instead free electrons, holes and excitons. In that case, pre-transition events must be taken into account as a source of processes competitive with the radiative decay of the excitation. These processes must generally include the migration of the excitation that eventually results in electron/hole localization in traps, defect formation or thermalization at defect sites.

In fact, if on the one hand there are many studies which clarify the occurrence of exciton self-trapping in SiO_2 ²⁵, on the other hand there are also evidences of excitation migration in the amorphous network^{24,52–55}, as well as theoretical basis for a non-

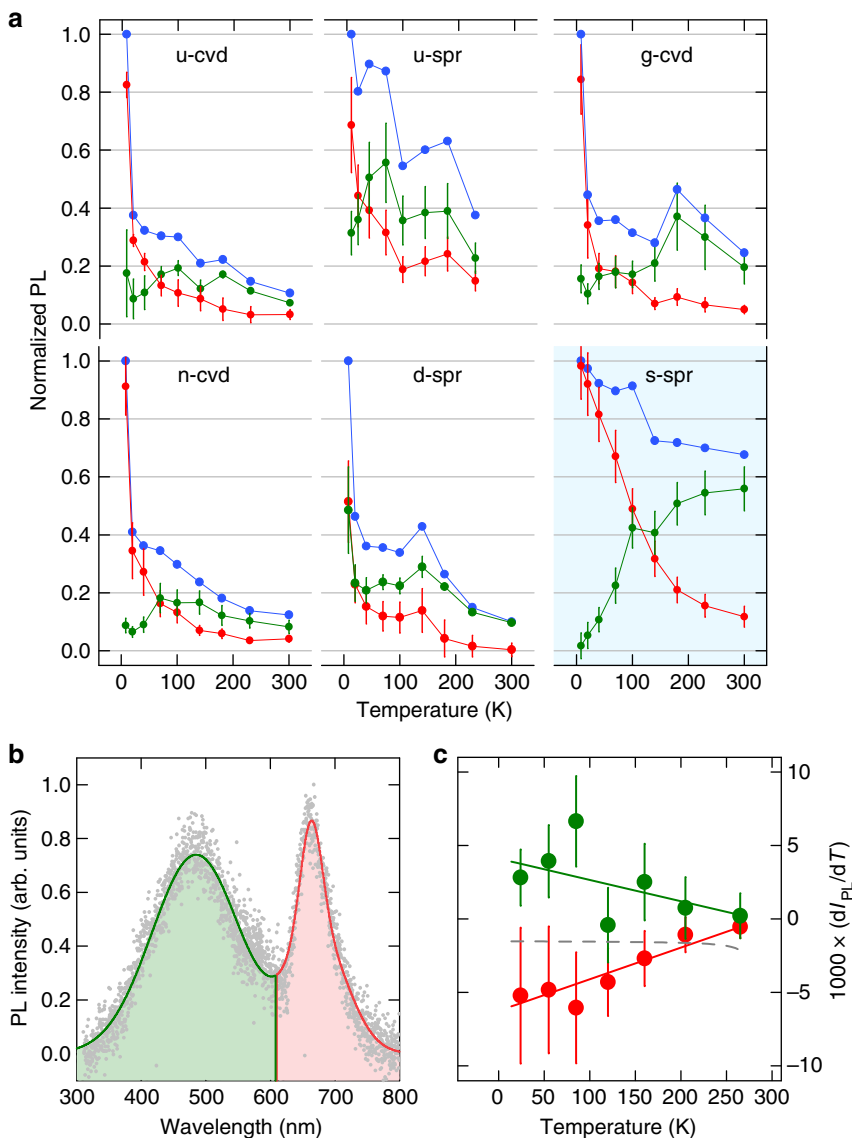


Fig. 3 Effects of competitive non-radiative decay. **a** Integrated intensity of the red and the green photoluminescence (red and green circles, respectively) excited at 13.8 eV as a function of temperature (8–300 K) for different silica systems (from left to right, starting from the top, pure synthetic commercial dry silica by chemical vapour deposition (u-cvd), fully densified pure sol-gel silica (u-spr), synthetic commercial dry silica by chemical vapour deposition with 2 mol% GeO₂ (g-cvd), u-cvd material after neutron irradiation at a fluence of 10¹⁸ neutrons per cm² (n-cvd), sol-gel silica synthesized by addition of 1 mol% of Si₂(OCH₃)₆ as a molecular precursor of Si-Si groups defectiveness (d-spr), and fully densified sol-gel silica doped with 0.2 mol% SnO₂ (s-spr)). The uncertainty, estimated from the integrated noise-to-signal ratios of each spectrum, is reported as error bars for each experimental value. **b** Spectral ranges (indicated by red and green filled areas in a representative photoluminescence spectrum) used for the extraction of the integrated intensity data reported in **a** upon renormalization to the integrated intensity of the total photoluminescence spectrum at 8 K. **c** Relationship between the temperature dependency rates (dI_{PL}/dT) of the red and the green emissions (circles at negative and positive values, respectively) extracted from **a** for s-spr (highlighted by grey-shaded background); the uncertainty propagated from the noise-to-signal in I_{PL} data is reported as error bars. The linear regression of the data sets is reported as solid red and green lines. The dashed line indicates the slope ratio, which is nearly constant across the whole temperature range

null energy barrier and delay for exciton self-trapping in amorphous SiO₂^{21,22,56,57}. The available data indeed points to a non-null delay for exciton self-trapping in SiO₂⁵⁴, and to an excitation diffusion length for the self-trapped exciton too (via hopping migration) of the order of 10¹ nm²⁴. Noteworthy, the mobile nature of excitation in SiO₂ is also consistent with the analysis of the spectral shape of the exciton absorption peak at 10.2 eV⁵⁸. Accordingly, the progressive drop of the total photoluminescence efficiency in all systems (blue symbols in Fig. 3a), except for the s-spr material (highlighted by grey shading) that is discussed in the next section, points to a non-

negligible role of thermally assisted exciton migration towards non-radiative trapping sites competing with the radiative decay.

A single origin for the red and green photoluminescence. In contrast to the silica systems discussed in the previous section, showing a drop of both their red and green emission bands with increasing temperature⁴¹, a strict anti-correlation between the two photoluminescence intensities is found for the s-spr material (Fig. 3a, c), which is unprecedented in the literature. Notably, the total spectrally integrated photoluminescence intensity is nearly temperature independent, compared with the other systems, and

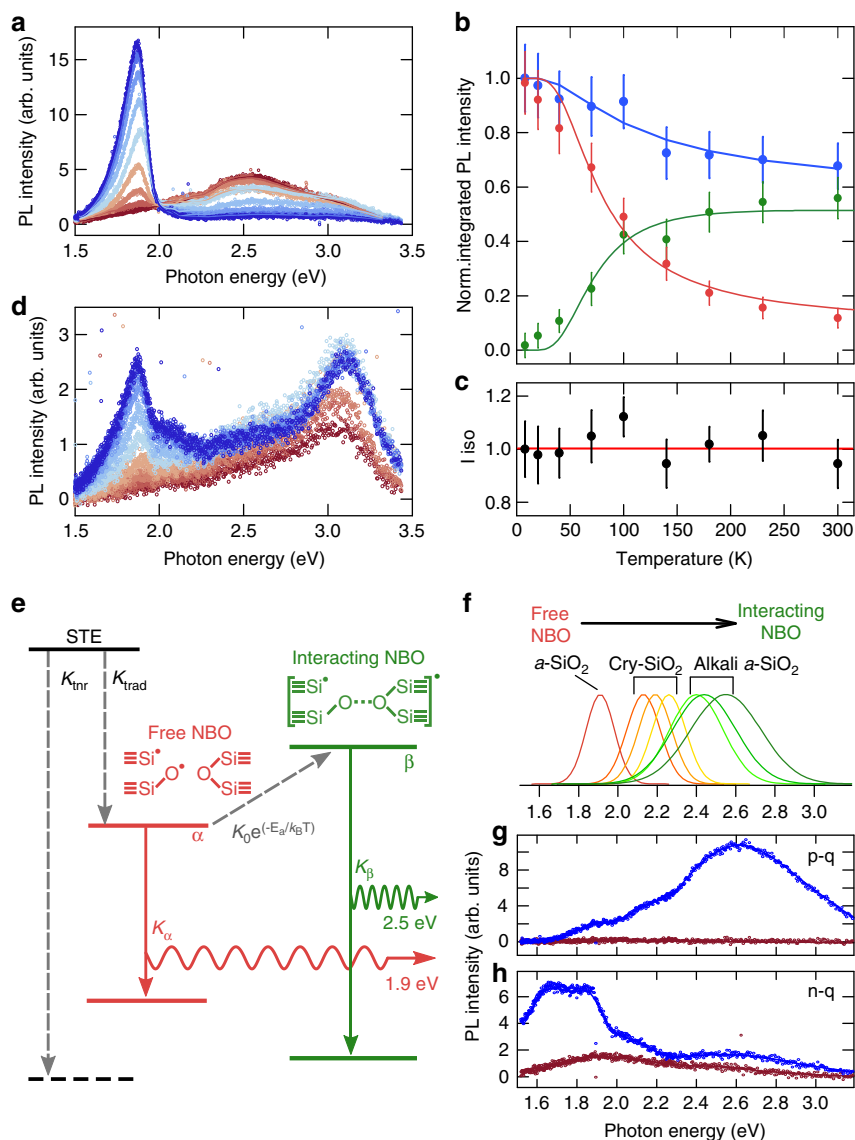


Fig. 4 Interconversion between red and green emissions. **a** Photoluminescence spectra excited at 13.8 eV, collected at different temperature from 8 to 300 K (from blue to red) in s-spr silica, showing an isostilbic point at 2.0 eV where photoluminescence intensity is independent of the temperature-induced changes of red and green components. **b** Integrated counts I of the emissions from α (red circles) or β (green circles) states, and their sum (blue circles) in s-spr sample; the uncertainty, estimated from the integrated noise-to-signal ratios of each spectrum, is reported as error bars for each experimental value; curves are fits of the data following the model described in the text with $k_{\text{trn}}/k_{\text{trad}} = K \exp(-E_{\text{nr}}/k_{\text{B}}T)$, with $K = 0.79 \pm 0.18$ and $E_{\text{nr}} = 12 \pm 3$ meV, and $k_{\text{isc}}/k_{\alpha} = K_0 \exp(-E_{\text{isc}}/k_{\text{B}}T)$, with $K_0 = 6.5 \pm 2.3$ and $E_{\text{isc}} = 16 \pm 3$ meV of activation energy for STE transition to β -state. **c** Temperature dependence of the photoluminescence intensity I_{iso} at the isostilbic point energy 2.0 eV, normalized to the low temperature value; the uncertainty, estimated from the integrated noise-to-signal ratios of each spectrum, is reported as error bars for each experimental value. **d** Spectra collected at different temperature from 8 to 300 K (from blue to red) on the same sample by exciting at 210 nm, below the energy gap. **e** Schematics of energy levels with radiative (continuous arrows) and non-radiative (dashed arrows) transitions involved in STE decay and subsequent relaxation to α or β excited levels responsible for red and green emissions, respectively; Kinetic rates are indicated as in the text. **f** Representative experimental or theoretical photoluminescence spectra of NBO variants including: free NBO³⁰, NBOs on crystal surfaces (cry-SiO₂)³⁶, and alkali-perturbed NBOs²⁷. **g** Photoluminescence spectra excited at 13.8 eV of pure synthetic quartz (p-q) at 8 K (blue curve) and 300 K (red curve). **h** Photoluminescence spectra excited at 13.8 eV of pure synthetic quartz after neutron irradiation (n-q) at 8 K (blue curve) and 300 K (red curve)

the thermal rates of the green and red emission intensity differ from each other only for a constant scale factor (about ~ 1.5) (Fig. 3c). These data suggest a decay kinetics in which the two emissions are not independent of each other, arising instead from the same kind of configuration undergoing one of two competitive transitions anticorrelated by some kind of intersystem crossing process. This interpretation is confirmed by the thermal evolution of the photoluminescence spectrum of the s-spr material in Fig. 4a that, being only weakly affected by non-

radiative decay losses (note the weak $\sim 20\%$ dimming of the spectrally integrated intensity between 8 and 300 K in Fig. 4b), provides direct insight into the local relaxation process of the STE. As a result of the suppression of quenching effects, the spectra vs. temperature in Fig. 4a reveal a clear-cut isostilbic point at 2.0 eV, where the photoluminescence intensity is constant at any temperature (Fig. 4c), despite the progressive shift of the spectral distribution of the emitted photons from the red band to the green component (Fig. 4b).

Importantly, sub-band-gap excited spectra do not show an isostilbic point (Fig. 4d). In this case, the spectra are dominated by the emission of NBO and Sn-variant of ODC at 1.9 eV and 3.1 eV⁴², respectively, with intensity decreasing at increasing temperature. An isostilbic point has non-zero probability to occur only when the luminescence spectrum arises from two states connected to each other by an interconversion process (see Supplementary Note 1)^{59,60}. Therefore, data in Fig. 4a reveal, for the first time, a common configurational origin of the two decay channels and identify a twofold relaxation process as local STE decay mechanism in SiO₂. The isostilbic point in Fig. 4a is also an indirect demonstration that radiation-induced NBOs, if any, do not contribute significantly to the emission spectra upon above-band-gap excitation, since they would otherwise give a spectral contribution at 1.9 eV uncorrelated with the 2.5 eV emission, inconsistently with the occurrence of an isostilbic point which instead highlights a pure intersystem crossing process. The energy scheme of the electronic states involved in such a thermally activated conversion process is sketched in Fig. 4e. According to this scheme, a photogenerated exciton is originally self-trapped into a ‘free NBO’ configuration (α state) that either decays radiatively by emitting a 1.9 eV photon (with rate k_α) or undergoes thermally assisted intersystem crossing (with rate k_{ISC}) to a slightly modified configuration (β), from which the green emission at 2.5 eV occurs with rate k_β . The moderate non-radiative effects responsible for the weak photoluminescence dimming with increasing temperature is accounted for by a competitive pathway, common to both the decay channels. We assign to this effect a rate $k_{nr} = K \exp[-E_b/k_B T]$ that can be determined from the spectrally integrated photoluminescence intensity vs. T in Fig. 4b. This effect is mainly driven by trapping in non-radiative defects occurring before exciton localization in the radiative sites, as discussed in the next section. Accordingly, thermally activated multi-phonon non-radiative channels competitive to radiative decay are expected to be negligible, as previously inferred^{25,33}. Within these assumptions, the intensity ($I_{R,G}$) of the red and the green emission can be expressed through the equation $I_{R,G} = C / \{1 + (K_0 \exp[-E_{isc}/k_B T])^n\}$, where $K_0 = k_{ISC}(T = \infty)/k_\alpha$, E_{isc} is the activation energy of the intersystem crossing process and $C = k_{trad}/[k_{trad} + k_{tnr}]$, where k_{trad} and k_{tnr} are, respectively, the radiative and non-radiative decay rate of trapped excitons. The exponent n is 1 for the red emission and -1 for the green band.

By using this model to fit the experimental data in Fig. 4b, we obtain an activation energy $E = 16 \pm 3$ meV, which is reasonably close to the recently discovered low-energy phonon mode (8 meV)³⁷ coupled to NBOs in SiO₂. This suggests that the inter-configurational $\alpha \rightarrow \beta$ conversion process might be promoted by a low-energy vibration, such as a NBO bending mode enhancing the interaction between a NBO and its surrounding atoms and thereby stabilizing the perturbed electronic density of the non-bridging moiety. Following this argument, the 1.9 eV and the 2.5 eV emissions seem to be ascribable to two NBO configurational variants. Accordingly, the green band is peaked at 2.5 eV, which is consistent with the emission energy of NBOs perturbed by the interaction with nearby groups^{27,36}. In Fig. 4f, we summarize the emission spectra, determined either experimentally or theoretically, for different NBO variants, including the ‘free NBO’ species reported in the original work by Skuja³⁰ and the NBOs perturbed by the interaction with nearby alkali ions found by Zatsopin et al.²⁷ in alkali-silicate glasses, which show progressively lower emission energy from 2.6 eV to 2.4 eV in the sequence Li \rightarrow Na \rightarrow K, according to the lower ionic field strength of cations with larger ionic radius. Accordingly, theoretical calculations on different types of SiO₂ surfaces

predicted larger transition energies for NBO groups interacting with nearby bridging oxygen atoms³⁶.

The observation of the red-emitting and green-emitting STEs being ‘unperturbed’ or ‘structurally perturbed’ variants of the same NBO centre has important consequences on our understanding of the optical behaviour of crystalline SiO₂. Specifically, it explains why the red emission from ‘non-interacting’ NBOs has never been observed in quartz, while it is commonly exhibited by amorphous or amorphized SiO₂ materials. The more compact structure of quartz with respect to the open network of amorphous silica promotes the interaction between NBOs and their surrounding lattice. As a result, exciton decay occurs exclusively through interacting NBOs, leading to the typical green luminescence band and no red emission by isolated NBOs. To verify this point, in Fig. 4g, h, we also report the band-to-band excited photoluminescence spectra of pure synthetic quartz, respectively before (sample p-q) and after (sample n-q) neutron irradiation. In agreement with the above interpretation, the pristine material exhibits photoluminescence in the green spectral region at 2.5–2.7 eV. On the other hand, upon partial amorphization by heavy neutron irradiation (at a fluence of 10^{18} cm⁻²)³⁶, the low temperature photoluminescence spectrum becomes dominated by a 1.6–1.8 eV red emission band compatible with the radiative decay of non-interacting NBOs, completely quenched at room temperature.

Radiative vs. non-radiative exciton decay. A further compelling consequence of the unique photophysical behaviour of the s-spr material in Figs. 2 and 3 is a potential strategy for designing SiO₂ networks with intrinsic excitations nearly unaffected by thermally assisted decay in non-radiative defects. Two possible factors could cause the insensitivity to thermal photoluminescence quenching of the s-spr system: (i) a low density of non-radiative defects and (ii) the occurrence of strongly competitive mechanisms of radiative decay in regular sites, absent in other SiO₂ variants, promoted by local perturbations caused by substitution of regular Si sites by Sn atoms. Such dopant-related effect would enhance the exciton localization without preventing excitons from recombining radiatively. Figure 5a shows a schematic depiction of this latter scenario. Figure 5b depicts the situation in a highly defective network without preferential paths for radiative recombination in alternative decay sites.

Both such situations can be described by a photoluminescence quantum efficiency, $\eta_r = (k_{irad} + k_{srad}) / (k_{irad} + k_{srad} + k_{def})$, determined by three exciton decay rates, respectively in intrinsic radiative sites (k_{irad}), substituted radiative sites (k_{srad}) and non-radiative defects (k_{def}), each of which assumes different values depending on the relative concentration of the respective sites. Specifically, the different rates, k_j with $j = irad, srad, def$, can be expressed as $k_j = n_j v_j d \sigma_j$, where v_j and d are respectively the frequency and the step length of the exciton hopping process and n_j and σ_j are the number density and cross section of the j -th type of site. The term, $v_j = v_0 \exp[-(\epsilon_j - \epsilon_0)/k_B T]$ accounts for the thermally activated hopping from a regular site (with energy ϵ_0) to an adjacent perturbed site (with energy ϵ_j), resulting in non-nil activation energy $\Delta\epsilon_j = \epsilon_j - \epsilon_0$ for hopping in perturbed sites. In turn, $n_j \sim R_j^{-3}$ where R_j is the mean distance between neighbouring sites, as sketched in Fig. 5a, b.

This approach yields a temperature-dependent photoluminescence quantum yield $\eta_r(T) = (1 + S a e^{-\Delta\epsilon/k_B T}) / (1 + a e^{-\Delta\epsilon/k_B T})$, where $S = n_{srad} / (n_{srad} + n_{def})$ expresses the balance between the relative abundance of substituted radiative and non-radiative decay sites sampled by an exciton. For concentration of non-radiative decay sites much lower than radiative ones, corresponding to $S \sim 1$, the expression describes a situation of nearly T -independent η_r . On the

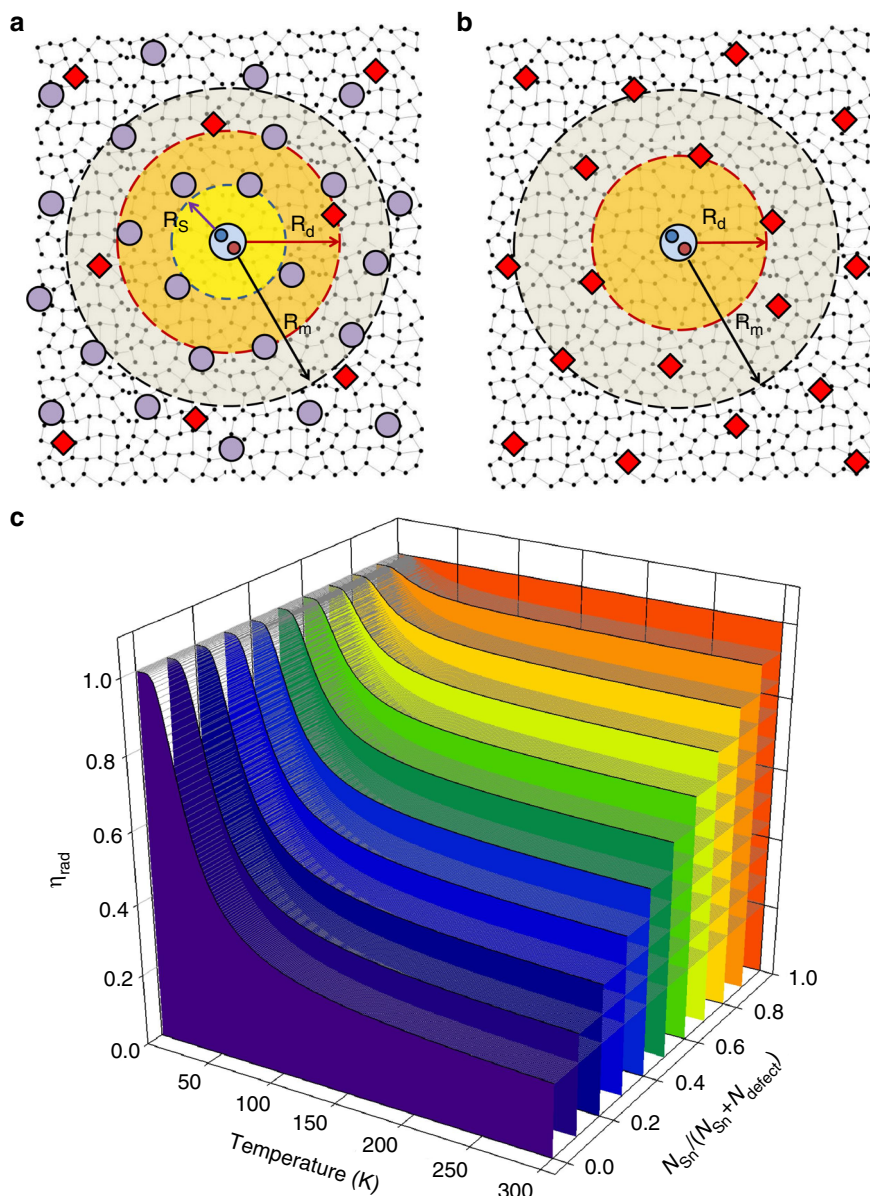


Fig. 5 Exciton trapping paths. **a** Schematics 2D representation of an amorphous network (points connected by sticks) with a concentration of non-radiative defects (red diamonds) lower than the concentration of substituted sites characterized by large trapping cross section and high rate of radiative recombination (grey circles). R_s and R_d are the mean distances an exciton (at the centre) has to travel before finding substituted sites or defects, respectively. **b** Representation of an opposite situation of a network with large defectiveness and no site of preferential trapping and radiative decay. R_m represents the mean free path of exciton in the unperturbed network. In s-spr material, the calculated R_s and R_d values are about 5 and 9 nm, respectively, while R_m in SiO_2 was estimated to range from 30 to 300 nm²⁶. **c** Temperature dependence of the quantum yield η_{rad} at different ratios between radiative and non-radiative traps, in the case of trap density $n_{\text{srad}} + n_{\text{def}} = 0.1 \text{ mol\%}$, $\Delta\epsilon/k_B = 70 \text{ K}$, and $\sigma_{\text{traps}} = 70\sigma_{\text{rad}}$, with $\Delta\epsilon_{\text{srad}} = \Delta\epsilon_{\text{def}} = \Delta\epsilon$, $\sigma_{\text{srad}} = \sigma_{\text{def}} = \sigma_{\text{traps}}$

other hand, for larger fractions of non-radiative sites ($S \sim 0$), η_r experiences severe temperature quenching. These scenarios are exemplified in Fig. 5c, where the total concentration ($n_{\text{srad}} + n_{\text{def}}$) of radiative and non-radiative perturbed sites is kept constant at 0.1 mol% of the total intrinsic network sites, whereas the other parameters are adjusted to reproduce the strongly thermally quenched behaviour of the heavily defective undoped material (e.g. n-cvd in Fig. 3a). Interestingly, by comparing Fig. 5c with the weak thermal dependence of the total emission intensity of the s-spr material in Fig. 4c, we find that the concentration of radiative decay sites must be just below $S = 1$ (~ 0.7 – 0.8), which is compatible with the expected concentration of regularly coordinated Sn-substituted sites (see below).

The experimental data on s-spr material shown in Fig. 4 are compatible with the situation depicted in Fig. 5a, where thermally activated exciton decay in non-radiative sites plays a negligible role with respect to localization in radiative centres. In order to experimentally validate this interpretation, we combine the optical absorption spectra of coordination defects in the near-UV with reflectivity spectra in the spectral region of the excitonic peak. We note that the relatively low density of non-radiative defects in s-spr material from the analysis in Fig. 5 suggests that Sn-doping does not relevantly increase the defect concentration, particularly twofold coordinated defects. Accordingly, the s-spr material shows a relatively small absorption coefficient of $\sim 3 \text{ cm}^{-1}$ at 5 eV (Supplementary Figure 1), corresponding to

twofold coordinated defects with concentration of $\sim 10^1$ ppm (considering an oscillator strength $f = 10^{-1}$)²⁸. This ‘lattice curing’ effect is typical of dopants introduced during sol-gel synthesis, where the occurrence of coordination defects at cation sites is strongly reduced with respect to CVD processes^{40,42}, as in Ge-doped sol-gel silica⁶¹. As a result, in the s-spr material, the concentration of non-radiative cationic defects is approximately an order of magnitude smaller than Sn sites and $S \sim 1$. Considering a 1 nm^3 cell containing 24 cations (consistently with density of silica^{20,21}), the resulting distance between two neighbouring Sn sites is less than six steps in the cation sublattice, which makes exciton localization in non-radiative defects statistically less probable with respect to localization in Sn-substituted sites. The analysis of the excitonic peak in the reflectivity spectra further indicates that Sn-substituted sites have a significantly larger cross section with respect to the intrinsic sites, which enhances their ability to act as localization sites for radiative decay with respect to exciton migration to non-radiative traps.

Reflectivity spectra and exciton bandwidth. Efficient exciton localization at Sn sites is expected to involve relevant fluctuations of the local potential, which should result in a measurable broadening of the excitonic reflectivity peak. The comparison between reflectivity spectra of the silica variants, including data extracted from the literature^{58,62–64}, is reported in Fig. 6a. We fitted the reflectivity profiles starting from the real and imaginary parts of the dielectric function $\epsilon(E)$, which we described through the superposition of a fixed number of Lorentzian contributions strictly corresponding to recognizable features in the reflectivity spectra (Fig. 6b, Supplementary Note 2 and Supplementary Table 2)⁶⁵. Notably, the model reproduces the exciton peak at $\sim 10 \text{ eV}$ in all investigated cases with a lorentzian function (solid curves in Fig. 6a), consistently with the assumption of exciton migration⁶⁶. Fundamentally for our discussion, the spectral position, E_{exc} and linewidth, Γ , values of the excitonic reflectivity peak are spread between 10.15–10.45 eV and 0.20–0.27 eV, respectively, which is likely the result of different fluctuations of the local potential between the various silica systems.

Importantly, by plotting the values of Γ as a function of E_{exc} (Fig. 6c), we find that the two parameters are inversely proportional to each other in a seemingly general linear relationship. This result resembles the observation of the mutual relationship between Γ and E_{exc} as a function of the temperature by Schreiber and Toyozawa⁶⁶, who found that Γ and E_{exc} are both determined by the thermal activation of lattice vibrations (dynamic response). The resulting temperature dependence is expressed through the equations, $\Gamma(T) = \Gamma_0 + \gamma T^n$ and $E_{\text{exc}}(T) = E_0 - \epsilon T$, where n is an exponent close to unity (ranging from 1 to 1.5 as a function of decreasing temperature) and Γ_0 and E_0 are temperature-independent contributions to the two quantities. On the other hand, when comparing materials with different structure or composition at a constant temperature as in Fig. 6c, the sample-to-sample variations of Γ and E_{exc} describe different ‘static’ sources of potential fluctuation within each silica network. Static disorder has been shown to influence the hole trapping process in silica⁶⁷. However, to date, no similar effect has been reported for the SiO_2 exciton. Analogously to the ‘dynamic’ description, we can describe the static contribution to Γ and E_{exc} through the temperature-independent linewidth $\Gamma_0 = \tilde{\Gamma}_0 + \tilde{\gamma}\Theta^n$ and peak energy $E_0 = \tilde{E}_0 - \tilde{\epsilon}\Theta$, where Θ is a generalized configurational temperature accounting for the structural characteristics of the different silica variants due to synthesis and treatment conditions and $\tilde{\Gamma}_0$ and \tilde{E}_0 are constants. Through this approach, the potential fluctuation due to static disorder yields a

quasi-linear Θ -dependence of both Γ and E_{exc} . As a result, at a given temperature T , the exciton bandwidth and peak energy in structurally different SiO_2 systems are mutually connected by a linear relationship $\Gamma = -aE_{\text{exc}} + b$ (with $a, b > 0$) where, for $n = 1$, $a = \tilde{\gamma}/\tilde{\epsilon}$ corresponds to the rate $(\partial\Gamma_0/\partial E_0)$ of structure-dependent broadening caused by changes in the structure-dependent shift of the exciton peak energy. In agreement with our analysis, the plot in Fig. 6c shows the general linear relationship between the exciton peak linewidth and energy, demonstrating the role of disorder in trapping excitons in silica. Notably, the theoretical curve calculated using $a = 0.163$ and $b = 1.91 \text{ eV}$ fits almost 90% of the data for undoped silica materials within a standard deviation of 1.6, as expected for a normal distribution.

A further, and possibly more compelling, aspect emerging from Fig. 6c is that, for the partially Sn-substituted system, where exciton decay in Sn sites is strongly favoured with respect to other network sites, both Γ and E_{exc} deviate by over 3σ from the linear relationship. The deviation consists in a much larger Γ (or E_{exc}) than expected at the observed E_{exc} (or Γ). Actually, substitution of Si by Sn atoms (with larger electron density) can hardly be a source of energy gap widening, rather the opposite, since SnO_2 has a much narrower gap than silica, even in nanostructured materials⁶⁸. Therefore, the observed deviation suggests a different source, other than the intrinsic topological disorder, of line broadening. This source is likely associated to fluctuations of the local potential at Sn sites, contributing to the amplitude, D , of lattice displacement. The parameter Γ is, indeed, proportional to D^2/B , where B is a measure of the exciton energy band⁶⁶. Since Sn sites are a minor fraction of the network sites, the exciton energy band is expected to be only weakly perturbed by Sn doping, with the system essentially behaving as an intrinsic network, leaving as the only effect of doping a relevant spectral broadening⁶⁶. Figure 6c constitutes the first experimental confirmation of Schreiber–Toyozawa calculations of impurity effects on the excitonic spectrum in SiO_2 ⁶⁹.

Discussion

The above analysis shows that, side-by-side investigations by means of synchrotron radiation excited photoluminescence and reflectivity experiments on a comprehensive collection of silica and quartz variants from different synthesis and processing conditions has enabled us to capture an unconventional perspective on generalities and peculiarities of SiO_2 -based systems. Specifically, in Sn-doped sol-gel silica with strongly suppressed non-radiative decay channels, we identified unprecedented fingerprints of double configuration in the interband-excited green luminescence previously ascribed to self-trapped exciton that could not be observed in other silica systems due to the dominant effect of non-radiative trapping processes. The in-depth analysis of the origin of such dual radiative response revealed a relationship between the exciton peak position and bandwidth in SiO_2 systems, which are parametrically linked to each other by structural effects on the exciton mobility and trapping processes. Such relationship, validated by experimental data acquired by us and extracted from representative literature reports, provides guidelines for the future design of silica-based materials with tailored optical properties by rational engineering of the material structure, with potential applicative impact on VUV technologies. Finally, taken together, our results offer an insight into the photophysical mechanisms responsible for the apparent absence of non-bridging oxygen centres in quartz. The evidence of the interplay between free and interacting non-bridging oxygens in the radiative exciton decay process, unambiguously identifies NBO as the elementary and fundamental player in radiation-induced bond-breaking events in all known varieties of silicon

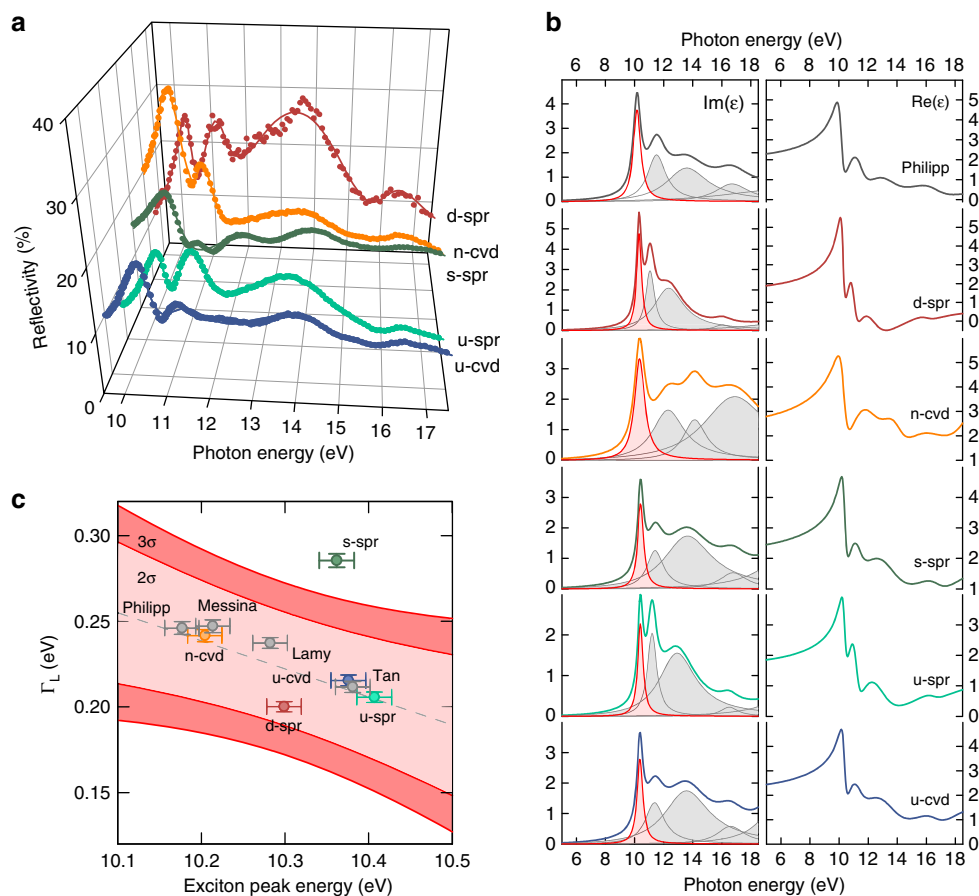


Fig. 6 Reflectivity spectra. **a** Reflectivity spectra (points) of different silica samples: from back to front, in sol-gel silica synthesized by addition of 1 mol% of $\text{Si}_2(\text{OCH}_3)_6$ as a molecular precursor of Si-Si groups defectiveness (d-spr), pure synthetic commercial dry silica by chemical vapour deposition after neutron irradiation at a fluence of 10^{18} neutrons per cm^2 (n-cvd), fully densified sol-gel silica doped with 0.2 mol% SnO_2 (s-spr), fully densified pure sol-gel silica (u-spr), and pure synthetic commercial dry silica by chemical vapour deposition (u-cvd); fit of the experimental data by means of the expression of the reflectivity R as a function of real and imaginary parts of the complex dielectric function $\epsilon(E)$ are shown by solid lines. **b** Imaginary (left side panel) and real (right side panel) parts of $\epsilon(E)$ (curves on the left and on the right, respectively), obtained as sum of Lorentzian components with spectral position and width extracted from the fit of the reflectivity data in **a**. Data from literature (Philipp) are also reported for comparison. **c** Spectral bandwidth, Γ_L , as a function of the respective peak position energy of the exciton component at ~ 10.3 eV (peaks in red in $\text{Im}(\epsilon)$ in **b**). Values obtained from literature reports are also reported and labelled by the first author's name of the respective study. The dashed lines indicate the result of the linear regression of the data. The shadowed areas are the regions of confidence corresponding to 2σ and 3σ deviations. The same colour code applies throughout the figure

dioxide, with a range of emission energies depending on the specific interaction with the nearby structural environment.

Methods

Materials. The set of investigated samples comprises silica and quartz from different sources, either commercial or synthesized in our laboratory by sol-gel methods, and with different kinds of perturbation, by post-synthesis treatments or doping processes. All samples were polished to optical grade with a final thickness between 0.2 and 1.2 mm depending on the sample. The description of the investigated samples—with the labels used in the text—with details on synthesis and/or treatment is given below. Information on structural and optical features, as we obtained by spectroscopic measurements (Supplementary Figure 1), are described in Supplementary Table 1. Sample u-cvd (undoped silica by CVD) is Tetrasil SE material purchased from Quartz & Silice, France. It is a type IV dry silica by vapour phase oxidation of SiCl_4 in water-free oxygen/argon plasma torch. Sample w-cvd (wet silica by CVD) is Tetrasil B material purchased from Quartz & Silice, France. It is a type III wet silica by hydrolysis of SiCl_4 sprayed into a hydrogen-oxygen flame. Sample g-cvd (Ge-doped silica by chemical vapour-deposition) is Ge-doped silica from an optical fibre preform purchased from Fibre Ottiche Sud, Italy. It is a type IV dry silica by modified chemical vapour deposition of SiCl_4 and GeCl_4 in oxidizing atmosphere. The germanium content is 2% mol. Sample p-q (pure quartz crystalline sample) is quartz from a Sawyer Premium Q single crystal bar prepared by hydrothermal growth. Samples were cut perpendicular to the optical axis. Samples n-q and n-cvd (neutron-irradiated samples) are obtained from p-q and u-cvd by neutron irradiation using a Triga Mark II reactor (Casaccia, Italy) with a

fluence of 10^{18} neutrons per cm^2 . Sample u-spr (undoped silica by solution-processing route) is pure silica by solgel. It was obtained by preparing in a polypropylene container 12 mL of a solution of ethanol (EtOH), tetraethoxysilane (TEOS) and water⁷⁰. The relative molar ratio of the precursors $\text{Si:H}_2\text{O:EtOH}$ was 1:7.4:10.7. The container was then sealed and put into a thermostatic chamber at 40 °C. The container cap was pierced so as to allow slow evaporation of the solvent. After 15 days of ageing, the obtained xerogel was sintered according to the following process: heating under oxygen atmosphere up to 105 °C (heating rate 10 °C h^{-1}) and maintained for 4 h; heated under oxygen atmosphere up to 450 °C (heating rate 10 °C h^{-1}) and maintained for 2 days; heated in vacuum (1.33 Pa) up to 950 °C (heating rate 4 °C h^{-1}); heated under oxygen atmosphere up to 1050 °C (heating rate 4 °C h^{-1}) and maintained for 20 h. Starting from this method the following modified solgel samples were prepared: Sample u2-spr (silica by solution-processing route with acetylacetone) is a variant of pure silica solgel sample by using the method described for u-spr and adding in the solution acetylacetone (acacH), with a final molar ratio $\text{Si:H}_2\text{O:EtOH:acacH}$ of 1:7.4:7.6:3. Sample d-spr (silica doped with 1% mol of Si-Si by solution-processing route) is defective silica intentionally doped with oxygen deficiency centres (ODC). It was prepared by the same method described for u-spr and adding, in the starting solution, 1% mol l of hexamethoxydisilane, a precursor containing the Si-Si group. Sample s-spr (silica doped with 0.2% mol of Sn by solution-processing route) is tin-doped solgel silica by the same method described for u-spr and adding 0.2% mol of dibutyl tin diacetate as Sn precursor. Sample f-spr (silica doped with 2% mol of F by solution-processing route) is fluorine doped solgel silica by the same method described for u-spr and adding 2% mol of triethoxyfluorosilane as F precursor. Sample e-spr (silica doped with 0.5% mol of Er by solution-processing route) is erbium doped

solgel silica by the same method described for u-spr and adding 0.5% mol of erbium (III) nitrate as Er precursor.

Measurements. Reflectivity and photoluminescence (PL) measurements were carried out in ultra-high vacuum with synchrotron radiation at the SUPERLUMI experimental station of HASYLAB at DESY (Hamburg, Germany). The incident beam spectral bandwidth was 0.3 nm, pulse width 130 ps, interpulse 192 ns. The reflected beam was collected, in near-normal geometry, by means of a photo-multiplier tube coated with sodium salicylate. Raw data were then corrected and scaled so as to account for the spectral distribution of the incident beam and to match silica reflectivity in the visible spectral region. PL were measured by integrating the signal detected with a charge-coupled device (CCD) coupled with a monochromator with a bandwidth of 3 nm. Data were corrected for the spectral dependence of the excitation intensity and spectral response of emission monochromator and detector. Low temperature measurements were collected after stabilizing the temperature with an accuracy of 1 K. Excitation-induced modification of the above-band-gap excited emission spectrum by possible defect generation was checked by comparing repeated spectral scans, collecting spectra in one shot by means of a polychromator and a CCD detector. No appreciable change was observed above the noise, both for acquisition time of minutes and for shorter exposure time, down to few seconds only. Details on the spectroscopic methods used in Raman, infra-red and near UV absorption measurements are reported in Supplementary Method 1.

Data availability

All data generated or analysed during this study are included in this published article and its Supplementary Information Files and are available from the corresponding author on reasonable request.

Received: 22 October 2017 Accepted: 28 September 2018

Published online: 25 October 2018

References

- Saika-Voivod, I., Poole, P. H. & Sciortino, F. Fragile-to-strong transition and polyamorphism in the energy landscape of liquid silica. *Nature* **412**, 514–517 (2001).
- Grigera, T. S., Martín-Mayor, V., G. Parisi, G. & Verrocchio, P. Phonon interpretation of the ‘boson peak’ in supercooled liquids. *Nature* **422**, 289–292 (2003).
- Zheng, K. et al. Electron-beam-assisted superplastic shaping of nanoscale amorphous silica. *Nat. Commun.* **1**, 24 (2010).
- Schiffrin, A. et al. Optical-field-induced current in dielectrics. *Nature* **493**, 70–74 (2013).
- Ferrera, M. et al. Low-power continuous-wave nonlinear optics in doped silica glass integrated waveguide structures. *Nat. Photon.* **2**, 737–740 (2008).
- Carmon, T. & Vahala, K. J. Visible continuous emission from a silica microphotonic device by third-harmonic generation. *Nat. Phys.* **3**, 430–435 (2007).
- Zhang, J., Gecevicius, M., Beresna, M. & Kazansky, P. G. Seemingly unlimited lifetime data storage in nanostructured glass. *Phys. Rev. Lett.* **112**, 033901 (2014).
- Tong, L. et al. Subwavelength-diameter silica wires for low-loss optical wave guiding. *Nature* **426**, 816–819 (2003).
- Brambilla, G. & Payne, D. N. The ultimate strength of glass silica nanowires. *Nano. Lett.* **9**, 831–835 (2009).
- Lancry, M. & Poumellec, B. UV laser processing and multiphoton absorption processes in optical telecommunication fiber materials. *Phys. Rep.* **523**, 207–229 (2013).
- Cellere, G. & Paccagnella, A. A review of ionizing radiation effects in floating gate memories. *IEEE Trans. Device Mater. Reliab.* **4**, 359–370 (2004).
- Weber, W. J. et al. Radiation effects in glasses used for immobilization of high-level waste and plutonium disposition. *J. Mater. Res.* **12**, 1946–1978 (1997).
- Griscom, D. L. A minireview of the natures of radiation-induced point defects in pure and doped silica glasses and their visible/near-IR absorption bands, with emphasis on self-trapped holes and how they can be controlled. *Phys. Res. Int.* **2013**, 379041 (2013).
- Kajihara, K., Hirano, M., Skuja, L. & Hosono, H. Intrinsic defect formation in amorphous SiO₂ by electronic excitation: Bond dissociation versus Frenkel mechanisms. *Phys. Rev. B* **78**, 094201 (2008).
- Hayes, W., Kane, M. J., Salminen, O., Wood, R. L. & Doherty, S. P. ODMR of recombination centres in crystalline quartz. *J. Phys. C: Sol. St. Phys.* **17**, 2943–2951 (1984).
- Tanimura, K., Tanaka, T. & Itoh, N. Creation of quasistable lattice defects by electronic excitation in SiO₂. *Phys. Rev. Lett.* **51**, 423–426 (1983).
- Itoh, C., Tanimura, K. & Itoh, N. Optical studies of self-trapped excitons in SiO₂. *J. Phys. C: Sol. St. Phys.* **21**, 4693–4702 (1988).
- Shluger, A. & Stefanovich, E. Models of the self-trapped exciton and nearest-neighbor defect pair in SiO₂. *Phys. Rev. B* **42**, 9664 (1990).
- Fisher, A. J., Hayes, W. & Stoneham, A. M. Structure of the self-trapped exciton in quartz. *Phys. Rev. Lett.* **64**, 2667–2670 (1990).
- Donadio, D. & Bernasconi, M. Ab initio simulation of photoinduced transformation of small rings in amorphous silica. *Phys. Rev. B* **71**, 073307 (2005).
- Van Ginhoven, R. M., Jónsson, H. & Corrales, L. R. Characterization of exciton self-trapping in amorphous silica. *J. Non-Cryst. Sol.* **352**, 2589–2595 (2006).
- Mott, N. F. Silicon dioxide and the chalcogenide semiconductors; similarities and differences. *Adv. Phys.* **26**, 363–391 (1977).
- Tanimura, K. & Itoh, N. Mechanisms of atomic processes induced by electronic excitation in solids. *Nucl. Instr. Meth Phys. Res. B* **33**, 815–819 (1988).
- Trukhin, A. N. Excitons in SiO₂: a review. *J. Non-Cryst. Sol.* **149**, 32–45 (1992).
- Song, K. S. & Williams, R. T. *Self-Trapped Excitons*. 270–299 (Springer-Verlag, Berlin/Heidelberg, 1993).
- Glinka, Y. D., Lin, S.-H. & Chen, Y.-T. Time-resolved photoluminescence study of silica nanoparticles as compared to bulk type-III fused silica. *Phys. Rev. B* **66**, 035404 (2002).
- Zatsepin, A. F., Guseva, V. B. & Zatsepin, D. A. Luminescence of modified nonbridging oxygen hole centers in silica and alkali silicate glasses. *Glass Phys. Chem.* **34**, 709–715 (2008).
- Skuja, L. Optically active oxygen-deficiency-related centers in amorphous silicon dioxide. *J. Non-Cryst. Sol.* **239**, 16–48 (1998).
- Skuja, L. Isoelectronic series of twofold coordinated Si, Ge, and Sn atoms in glassy SiO₂: a luminescence study. *J. Non-Cryst. Sol.* **149**, 77–95 (1992).
- Skuja, L. The origin of the intrinsic 1.9 eV luminescence band in glassy SiO₂. *J. Non-Cryst. Sol.* **179**, 51–69 (1994).
- Griscom, D. L. & Friebele, E. J. Fundamental defect centers in glass:²⁹Si hyperfine structure of the nonbridging oxygen hole center and the peroxy radical in a-SiO₂. *Phys. Rev. B* **24**, 4896 (1981).
- Hosono, H. et al. Vacuum ultraviolet optical absorption band of non-bridging oxygen hole centers in SiO₂ glass. *St. Commun.* **122**, 117–120 (2002).
- Vaccaro, L., Cannas, M. & Boscaino, R. Phonon coupling of non-bridging oxygen hole center with the silica environment: Temperature dependence of the 1.9 eV emission spectra. *J. Lumin.* **128**, 1132–1136 (2008).
- Cannas, M. & Gelardi, F. M. Vacuum ultraviolet excitation of the 1.9-eV emission band related to nonbridging oxygen hole centers in silica. *Phys. Rev. B* **69**, 153201 (2004).
- Suzuki, T. et al. Electronic structure of oxygen dangling bond in glassy SiO₂: the role of hyperconjugation. *Phys. Rev. Lett.* **90**, 186404 (2003).
- Giordano, L., Sushko, P. V., Pacchioni, G. & Shluger, A. L. Optical and EPR properties of point defects at a crystalline silica surface: ab initio embedded-cluster calculations. *Phys. Rev. B* **75**, 024109 (2007).
- Skuja, L., Kajihara, K., Grube, J. & Hosono, H. Luminescence of non-bridging oxygen hole centers in crystalline SiO₂. *AIP Conf. Proc.* **1624**, 130–134 (2014).
- Azzoni, C. B., Meinardi, F. & Paleari, A. Trapped-hole centers in neutron-irradiated synthetic quartz. *Phys. Rev. B* **49**, 9182 (1994).
- Makhov, V. N. et al. Multiplication of electronic excitations in nanophosphors Lu₂O₃:Eu³⁺ and Lu₂O₃:Tb³⁺. *J. Lumin.* **129**, 1711–1714 (2009).
- Takigawa, Y. et al. Surface alterations of SiO₂ optics by 9.8 and 8.5 eV laser photons. *J. Non Cryst. Solids* **125**, 107–116 (1990).
- Messina, F., Vaccaro, L. & Cannas, M. Generation and excitation of point defects in silica by synchrotron radiation above the absorption edge. *Phys. Rev. B* **81**, 035212 (2010).
- Chiodini, N. et al. Photoluminescence of Sn-doped SiO₂ excited by synchrotron radiation. *J. Non-Cryst. Sol.* **261**, 1 (2000).
- Martini, M., Meinardi, F., Paleari, A., Spinolo & Vedda, A. SiO₂:Ge photoluminescence: detailed mapping of the excitation-emission UV pattern. *Phys. Rev. B* **57**, 3718 (1998).
- Paleari, A., Chiodini, N., Di Martino, D. & Meinardi, F. Radiative decay of vacuum-ultraviolet excitation of silica synthesized by molecular precursors of Si-Si sites: an indicator of intra-center relaxation of neutral-oxygen-vacancies. *Phys. Rev. B* **71**, 075101 (2005).
- Meinardi, F. & Paleari, A. Native and radiation-induced photoluminescent defects in SiO₂: role of impurities. *Phys. Rev. B* **58**, 3511 (1998).
- Kawaguchi, Y. Time-resolved photoluminescence spectra of silica glass in a vacuum and nitrogen atmosphere. *Phys. Rev. B* **52**, 9224 (1995).
- Philipp, H. R. Optical properties of non-crystalline Si, SiO, SiO_x and SiO₂. *J. Phys. Chem. Sol.* **32**, 1935–1945 (1971).
- Hattori, T. Chemical structure of ultrathin silicon oxide films and the oxide-silicon interface, *Thin Sol. Films* **206**, 1–5 (1991).

49. Chiodini, N. et al. Sol-gel strategy for self-induced fluorination and dehydration of silica with extended VUV transmittance and radiation-hardness. *Chem. Mater.* **24**, 677–681 (2012).
50. Guzzi, M. et al. Neutron irradiation effects in amorphous SiO₂: optical absorption and electron paramagnetic resonance. *J. Phys. Cond. Matter* **5**, 8105–8116 (1993).
51. Anedda, A. et al. Vacuum ultraviolet absorption spectrum of photorefractive Sn-doped silica fiber preforms. *J. Non-Cryst. Sol.* **280**, 287 (2001).
52. Chiodini, N. et al. Ultraviolet photoluminescence of porous silica. *Appl. Phys. Lett.* **76**, 3209 (2000).
53. Stathis, J. H. & Kastner, M. A. Time-resolved photoluminescence in amorphous silicon dioxide. *Phys. Rev. B* **35**, 2972–2979 (1987).
54. Saeta, P. N. & Greene, B. I. Primary relaxation processes at the band edge of SiO₂. *Phys. Rev. Lett.* **70**, 3588–3591 (1993).
55. Guizard, S. et al. Time-resolved studies of carriers dynamics in wide band gap materials. *Nucl. Instr. Meth. Phys. Res. B* **116**, 43–48 (1996).
56. Mott, N. F. Recombination; a survey. *Sol. St. Electr.* **21**, 1275–1280 (1978).
57. Mott, N. F. & Stoneham, A. M. The lifetime of electrons, holes and excitons before self-trapping. *J. Phys. C: Solid State Phys.* **10**, 3391–3398 (1977).
58. Messina, F., Vella, E., Cannas, M. & Boscaino, R. Evidence of delocalized excitons in amorphous solids. *Phys. Rev. Lett.* **105**, 116401 (2010).
59. Greger, M., Kollar, M. & Vollhardt, D. Isosbestic points: How a narrow crossing region of curves determines their leading parameter dependence. *Phys. Rev. B* **87**, 195140 (2013).
60. Cohen, M. D. & Fischer, E. Isosbestic points. *J. Chem. Soc.* **2**, 3044–3052 (1962).
61. Chiodini, N., Meinardi, F., Morazzoni, F., Paleari, A. & Scotti, R. Optical transitions of paramagnetic Ge sites created by X-ray irradiation in oxygen-defect-free Ge-doped SiO₂ by the sol-gel method. *Phys. Rev. B* **60**, 2429–2435 (1999).
62. Philipp, H. R. Optical transitions in crystalline and fused quartz. *Solid State Commun.* **4**, 73–75 (1966).
63. Lamy, P. Optical constants of crystalline and fused quartz in the far ultraviolet. *Appl. Opt.* **16**, 2212–2214 (1977).
64. Tan, G. L., Lemon, M. F., Jones, D. J. & French, R. H. Optical properties and London dispersion interaction of amorphous and crystalline SiO₂ determined by vacuum ultraviolet spectroscopy and spectroscopic ellipsometry. *Phys. Rev. B* **72**, 2051172 (2005).
65. Christy, W. R. Classical theory of optical dispersion. *Am. J. Phys.* **40**, 1403–1419 (1972).
66. Schreiber, M. & Toyozawa, Y. Numerical experiments on the absorption lineshape of the exciton under lattice vibrations. I. The overall lineshape. *J. Phys. Soc. Jpn.* **51**, 1528–1536 (1982).
67. Yamaguchi, M., Saito, K. & Ikushima, A. J. Fictive-temperature-dependence of photoinduced self-trapped holes in a-SiO₂. *Phys. Rev. B* **68**, 153204 (2003).
68. Brovelli, S. et al. Fully inorganic oxide-in-oxide ultraviolet nanocrystal light emitting devices. *Nat. Commun.* **3**, 690 (2012).
69. Schreiber, M. & Toyozawa, Y. Numerical experiments on the absorption lineshape of the exciton under lattice vibrations. V. Impurities. *J. Phys. Soc. Jpn.* **53**, 864–872 (1984).
70. Chiodini, N. et al. Sol-gel synthesis of monolithic tin-doped silica. *J. Mater. Chem.* **9**, 2653–2658 (1999).

Acknowledgements

R.L. and A.P. acknowledge the financial support of Cariplo Foundation, Italy, under Project no. 2012–0920. S.B. thanks the European Community's Seventh Framework Programme (FP7/2007–2013) under Grant Agreement No. 226716 for financial support. We also acknowledge the previous works of synthesis by N. Chiodini and coworkers who produced the sol-gel silica samples we have selected for the present investigation to be compared with commercial silica.

Author contributions

A.P. conceived the project. A.P., F.M., S.B. and R.L. performed the experiments. A.P. and R.L. analysed and discussed the results. A.P. wrote the manuscript in consultation with all authors.

Additional information

Supplementary information accompanies this paper at <https://doi.org/10.1038/s42005-018-0069-5>.

Competing interests: The authors declare no competing interests.

Reprints and permission information is available online at <http://npg.nature.com/reprintsandpermissions/>

Publisher's note: Springer Nature remains neutral with regard to jurisdictional claims in published maps and institutional affiliations.



Open Access This article is licensed under a Creative Commons Attribution 4.0 International License, which permits use, sharing, adaptation, distribution and reproduction in any medium or format, as long as you give appropriate credit to the original author(s) and the source, provide a link to the Creative Commons license, and indicate if changes were made. The images or other third party material in this article are included in the article's Creative Commons license, unless indicated otherwise in a credit line to the material. If material is not included in the article's Creative Commons license and your intended use is not permitted by statutory regulation or exceeds the permitted use, you will need to obtain permission directly from the copyright holder. To view a copy of this license, visit <http://creativecommons.org/licenses/by/4.0/>.

© The Author(s) 2018